JOURNAL OF THERMOPHYSICS AND HEAT TRANSFER
Vol. 24, No. 4, October–December 2010

Entropy-Shock Interactions Using the Unified Flow Solver

Brook I. Bentley*
U.S. Air Force Research Laboratory, Albuquerque, New Mexico 87117
and
Robert B. Greendyke†
Air Force Institute of Technology, Dayton, Ohio 45433

DOI: 10.2514/1.47316

The unified flow solver, a hybrid continuum-rarefied code, is used to investigate the structure of a normal shock wave as an entropy perturbation is introduced upstream of the shock and allowed to propagate through the shock. The entropy spot is introduced into a two-dimensional domain over a range of Knudsen numbers ($Kn = 0.01$, 0.1, and 1.0) for Mach 2.0 in argon. Previous work on entropy-shock interactions has only been reported with an Euler-solution-method scheme. Here, results are presented in argon, using coupled Bhatnagar–Gross–Krook and Navier–Stokes solvers, using the hybrid nature of the unified flow solver code for a better examination and understanding of the propagation of entropy disturbances. Density, pressure, and temperature profiles, as well as the profiles of their gradients, are reported at discrete intervals after the entropy spot convects through the shock.

Nomenclature

$A^i_{l,r}$	=	local constants
a	=	radius of the entropy spot, m
C_{q_x}	=	heat flux coefficient
c_p	=	specific heat at constant pressure, J/kg · K
dV_c	=	volume element in velocity space, m^3/s^3
dV_x	=	volume element in physical space, m^3
E	=	energy, J
e	=	specific internal energy, J/kg
$\mathbf{F}^n_{i\pm1/2,j,k}$	=	flux on the cell face in the x direction
f	=	normalized velocity distribution function, s^3/m^3
f_x	=	partially integrated velocity distribution function in the axial direction
f_0	=	velocity distribution function at an initial moment
$\mathbf{G}^n_{i,j\pm1/2,k}$	=	flux on the cell face in the y direction
$H[\xi]$	=	Heaviside step function
$\mathbf{H}^n_{i,j,k\pm1/2}$	=	flux on the cell face in the z direction
h	=	nondimensional local cell size; specific enthalpy, J/kg
$I(f,f)$	=	collision integral, s^2/m^6
Kn	=	Knudsen number
K_r	=	rotational degrees of freedom
K_v	=	vibrational degrees of freedom
k	=	Boltzmann constant (1.38×10^{-23} kg · m^2/s^2 · K); coefficient of thermal conductivity, W/m · K
L	=	characteristic flow length, m
L_{ref}	=	reference length, m
m	=	molecular mass, kg
N	=	number of molecules in the system
$\mathbf{n}$	=	cell face unit outward normal vector
Pr	=	Prandtl number
p	=	pressure, N/m^2
Q	=	total heat flux, W/m^2
q_i	=	heat flux, W/m^2
R	=	specific gas constant, J/kg · K
$\Re^3$	=	set of all real numbers in three-dimensional space
r	=	radius from the center of the entropy spot, m
$\mathbf{r}$	=	position vector in physical space, m
S_{face}	=	face surface area in physical space, m^2
T	=	temperature, K; nondimensional temperature
T_n	=	normalized temperature
T'	=	temperature perturbation, K
t	=	time, s
U	=	nondimensional flow velocity
u	=	flow speed in the x direction, m/s
V	=	cell volume in physical space, m^3
V_{ref}	=	reference velocity, m/s
v	=	flow speed in the y direction, m/s
w	=	flow speed in the z direction, m/s
x	=	x-coordinate direction, m
x_c	=	x coordinate of the center of the entropy spot, m
$\mathbf{Y}^n_{ijk}$	=	cell-averaged value at time step n
y_c	=	y coordinate of the center of the entropy spot, m
Z_{rot}	=	rotational collision number
Z_{vib}	=	vibrational collision number
$\alpha^i_{l,r}$	=	local constants
γ	=	ratio of specific heats
$\Delta\xi_i$	=	velocity-space cell size, m/s
Δ_0	=	dimension for base cells, m (refinement level 0)
Δ_2	=	cell dimension for cells of refinement level 2, m
δ	=	inverse shock thickness
ε	=	perturbation amplitude
ζ_i	=	precollisional molecular velocity, m/s
ζ'_i	=	postcollisional molecular velocity, m/s
Θ_v	=	vibrational characteristic temperature, K
λ	=	mean free path, m
μ	=	dynamic viscosity, $N \cdot s/m^2$
ξ	=	velocity vector, m/s
ξ_i	=	velocity-space nodes
ρ	=	density, kg/m^3
ρ_n	=	normalized density
τ	=	intercollision relaxation time, s; nondimensional time
ψ	=	collisional invariants, $[1 \quad \boldsymbol{\xi} \quad \xi^2]$
ω	=	viscosity index

Subscripts

i	=	node in velocity space; cell node in physical space in the x direction

Presented as Paper 2009-1541 at the 47th AIAA Aerospace Sciences Meeting including The New Horizons Forum and Aerospace Exposition, Orlando, FL, 5–8 January 2009; received 22 September 2009; revision received 28 April 2010; accepted for publication 28 April 2010.

*First Lieutenant, Laser Effects Engineer; Brook.Bentley@kirtland.af.mil. Member AIAA.

†Associate Professor; Robert.Greendyke@afit.edu. Associate Fellow AIAA.

j = cell number in physical space; cell node in physical space in the y direction
k = time index; cell node in physical space in the z direction

Superscripts

n = time step
$*$ = intermediate time level

I. Introduction

REENTRY vehicles encounter complex flowfields that are difficult to solve using computational fluid dynamics (CFD). One part of the field may experience continuum flow (near stagnation points), while another part of the field may be rarefied (upstream of a shock or in an expansion region). Traditionally, Euler and Navier–Stokes (NS) continuum codes are used to solve for continuum flowfields, and rarefied solvers, such as direct simulation Monte Carlo (DSMC) and Boltzmann solvers, are used to solve for rarefied regions. Hybrid codes have been developed in an attempt to combine the efficiency of continuum solvers and the accuracy of rarefied solvers into one software package. The unified flow solver (UFS) [1–3] is a kinetic-based hybrid code meant to be more efficient than a DSMC code for near-continuum and transition flows and more accurate than Euler and NS solvers for transition and rarefied flows. UFS uses the Boltzmann equation to solve for the velocity distribution function (VDF) in each cell and then calculates the macroscopic flow quantities in each cell from the VDF.

Since UFS is a hybrid code, it can effectively handle flows with both continuum and rarefied regions by using an appropriate switching parameter, or continuum breakdown criterion. Kolobov et al. [2] suggest two switching parameters for the UFS hybrid code, based on either density gradients or pressure and velocity gradients. Using the correct switching parameter is important in UFS because, otherwise, nonpositive VDFs may be obtained, which is physically impossible [2]. Other switching parameters have been considered, such as the Knudsen number, defined as $Kn = \lambda/L$, or a switching parameter based on entropy [4,5]. One drawback of the latter parameter is that the more computationally expensive rarefied methods, such as DSMC, must first be used to calculate the entropy in order to determine whether the continuum assumptions still hold for that cell.

Besides determining continuum and rarefied (or kinetic) domains, a hybrid code must also choose an appropriate coupling method. Three classes of coupling have been considered to date [2]. The first decomposes the physical domain into kinetic and continuum subdomains. The second instead decomposes the velocity domain and separately considers fast and slow particles. The third calculates the VDF in all the cells and then uses that information to compute transport properties for the continuum equations. UFS takes the third approach.

This work reports the results of a new study on how an entropy spot (generated via a temperature or density perturbation) affects a two-dimensional shock in argon, using one of UFS's kinetic solvers for Knudsen numbers of 0.01, 0.1, and 1.0 at Mach 2.0. There are three basic modes of disturbance in a gas (acoustic or pressure, vortical, and entropy), and any disturbance can be decomposed into a linear combination of these three modes [6]. Initial studies beginning in the 1950s were focused on noise generation (acoustic effects), due to turbulence traveling through a shock, using a small vortex perturbation in the flow to simulate localized turbulence [7–13]. More recently, articles by Duck et al. have extended the freestream disturbance analysis to include acoustic, vortical, and entropy waves, analytically showing that, when any one of these disturbances travels through an oblique shock, all three modes are created downstream of the shock [14,15]. As discussed by Fabre and Jacquin, a cylindrical entropy spot can be decomposed, using Fourier synthesis into plane entropy waves arranged with different orientations [16]. Thus, an entropy spot traveling through a normal shock will excite acoustic, vertical, and entropy disturbances downstream of the shock.

Hussaini and Erlebacher [17] provide multiple reasons why entropy-shock interactions are important in aerospace applications, such as turbulence amplification in shock-turbulent boundary-layer interactions, density fluctuations in supersonic wake-shock interactions, noise generation in hot rocket exhausts with oblique shock waves, and enhanced mixing caused by shock interactions in the combustor of a scramjet engine with hot and cold flows (oxidant and fuel). Numerical studies to date have been performed on entropy-shock interactions using two-dimensional Euler schemes only [6,16–18]. This work presents a new study, using the NS equations in the UFS kinetic solver to examine this problem. The present work is a continuation of a prior study by Bentley [19], wherein he attempted to use the NS equations in the UFS kinetic solver to study entropy-shock interactions. However, this work has eliminated the symmetry boundary effects in the UFS simulations by extending the analysis to the full (rather than half) domain.

II. Unified Flow Solver

UFS uses both continuum and kinetic solvers when computing flow parameters. The user can specify which solvers to use and where in the domain they should be called. The kinetic solvers are either approximations of the Boltzmann equation [such as the Bhatnagar–Gross–Krook (BGK) model] or a direct numerical simulation of the collision integral using some intermolecular force model. As of 2006, four intermolecular force models have been included in UFS, namely, the hierarchical statistical model, the inverse power repulsive potential, the Lennard–Jones potential, and the Coulomb potential [2]. The UFS code is capable of parallel computing, using the message-passing interface library. It uses Cartesian quadtree (two-dimensional) or octree (three-dimensional) grids, meaning that all cells are either squares or cubes, for which the dimensions only differ by some factor of two.

The Boltzmann equation describes how the VDF evolves in time and space and can be framed in the following form when neglecting external forces:

$$\frac{\partial f}{\partial t} + \nabla_{\mathbf{r}} \cdot (\xi f) = I(f, f) \tag{1}$$

The term on the right-hand side is called the collision term, or the collision integral, because its direct calculation involves multidimensional integration. See Harris [20] for an introduction to how the Boltzmann equation can be arrived at from the more general Liouville equation. To solve Eq. (1) numerically, a Cartesian mesh is created in velocity space with nodes ξ_i and cell sizes $\Delta\xi_i$. Using this mesh, Eq. (1) can be reduced to a system of linear hyperbolic equations in physical space with the nonlinear source term

$$\frac{\partial f_i}{\partial t} + \nabla_{\mathbf{r}} \cdot (\xi_i f_i) = I(f_i, f_i) \tag{2}$$

where the subscript i indicates that the parameter is evaluated at nodes i. The UFS uses only Cartesian grids in physical space.

Equation (2) is solved in two stages: collisionless flow and relaxation, divided by an intermediate time stage. For the collisionless flow stage, the collision integral is assumed to be zero, and an explicit finite-volume scheme is used:

$$V\frac{f_{ij}^{*k} - f_{ij}^{k-1}}{\Delta t} + \sum_{\text{face}} (\xi_i \cdot \mathbf{n})_{\text{face}} f_{i,\text{face}}^{k-1} S_{\text{face}} = 0 \tag{3}$$

To calculate $f_{i,\text{face}}^{k-1}$, interpolation schemes are used (either first- or second-order), with three options for the second-order limiter: none, minmod, or van Leer. The minmod limiter, which is the most conservative of the second-order limiters, is used in this study.

For the relaxation stage,

$$\frac{f_{ij}^{k} - f_{ij}^{*k}}{\Delta t} = -\nu_{ij}^{*k} f_{ij}^{*k} + \Phi_{ij}^{*k} \tag{4}$$

Similar to the BGK model, UFS replaces the complex collision integral with two terms ($-\nu f$ and Φ), providing a similar relaxation to equilibrium as is inherent in the BGK model.

Since microscopic flow parameters can be obtained through the moments of the VDF, the continuum solvers are also based on the Boltzmann equation. Additionally, coupling of the continuum and kinetic solvers is less computationally intensive when they are all based on the Boltzmann equation. A general description of the Euler and NS solver methodology in UFS follows.

The Euler equations can be presented in the form

$$\frac{\partial \mathbf{Y}}{\partial t}+\frac{\partial \mathbf{F}}{\partial x}+\frac{\partial \mathbf{G}}{\partial y}+\frac{\partial \mathbf{H}}{\partial z}=0 \tag{5}$$

where

$$\begin{bmatrix}\mathbf{Y}\\ \mathbf{F}\\ \mathbf{G}\\ \mathbf{H}\end{bmatrix}= \begin{bmatrix}\rho & \rho u & \rho v & \rho w & E\\ \rho u & p/2+\rho u^2 & \rho uv & \rho uw & u(E+p)\\ \rho v & \rho uv & p/2+\rho v^2 & \rho vw & v(E+p)\\ \rho w & \rho uw & \rho vw & p/2+\rho w^2 & w(E+p)\end{bmatrix} \tag{6}$$

where the energy is defined as $E=\frac{3}{2}\rho T+\rho(u^2+v^2+w^2)$, and the pressure $p=nkT$. Discretizing Eq. (5) with an explicit finite-volume scheme, and moving spatial derivatives to the right-hand side,

$$\frac{\mathbf{Y}^{n+1}_{ijk}-\mathbf{Y}^{n}_{ijk}}{\Delta t}=-\left(\frac{\mathbf{F}^{n}_{i+1/2,j,k}-\mathbf{F}^{n}_{i-1/2,j,k}}{\Delta x}+\frac{\mathbf{G}^{n}_{i,j+1/2,k}-\mathbf{G}^{n}_{i,j-1/2,k}}{\Delta y}+\frac{\mathbf{H}^{n}_{i,j,k+1/2}-\mathbf{H}^{n}_{i,j,k-1/2}}{\Delta z}\right) \tag{7}$$

The fluxes are calculated using moments of the distribution function:

$$\begin{aligned}\mathbf{F}_{i\pm1/2,j,k}&=\frac{1}{\Delta t}\int_{t^n}^{t^{n+1}}\int_{\Re^3}\psi\xi_x f(x_{i\pm1/2},y_j,z_k,t,\xi)\,\mathrm{d}\xi\,\mathrm{d}t\\ \mathbf{G}_{i,j\pm1/2,k}&=\frac{1}{\Delta t}\int_{t^n}^{t^{n+1}}\int_{\Re^3}\psi\xi_y f(x_i,y_{j\pm1/2},z_k,t,\xi)\,\mathrm{d}\xi\,\mathrm{d}t\\ \mathbf{H}_{i,j,k\pm1/2}&=\frac{1}{\Delta t}\int_{t^n}^{t^{n+1}}\int_{\Re^3}\psi\xi_z f(x_i,y_j,z_{k\pm1/2},t,\xi)\,\mathrm{d}\xi\,\mathrm{d}t\end{aligned} \tag{8}$$

The collisional invariants are so named because they have the property

$$\int_{\Re^3}\psi I(f,f)\,\mathrm{d}\xi=0$$

A more detailed description of the collisional invariants can be obtained in the work by Sone [21]. The VDFs at the cell faces are calculated as

$$f(x_{i+1/2},y_j,z_k,t,\xi)=H[\xi_x]f_l^{\mathrm{eq}}+(1-H[\xi_x])f_r^{\mathrm{eq}}$$

where f_l^{eq} and f_r^{eq} are the equilibrium VDFs on the cell's left and right faces, respectively,

$$\begin{aligned}f_l^{\mathrm{eq}}&=\frac{\rho_{i-1/2}}{(\pi T^n_{i-1/2})^{3/2}}\exp\left[-\frac{(\xi_x-u_{i-1/2,j,k})^2+(\xi_y-v_{i-1/2,j,k})^2+(\xi_z-w_{i-1/2,j,k})^2}{T^n_{i-1/2}}\right]\\ f_r^{\mathrm{eq}}&=\frac{\rho_{i+1/2}}{(\pi T^n_{i+1/2})^{3/2}}\exp\left[-\frac{(\xi_x-u_{i+1/2,j,k})^2+(\xi_y-v_{i+1/2,j,k})^2+(\xi_z-w_{i+1/2,j,k})^2}{T^n_{i+1/2}}\right]\end{aligned} \tag{9}$$

and $H[\xi]$ is the Heaviside step function:

$$H[\xi]=\begin{cases}1, & \xi>0\\ 0, & \xi\le 0\end{cases} \tag{10}$$

Hence, the Euler kinetic scheme uses only Maxwellian VDFs, which is consistent with the zeroth-order Chapman–Enskog expansion. If a Boltzmann solver is being used in a neighboring cell, then the parameters required for the calculation of f_l^{eq} or f_r^{eq} are found from moments of the VDF in the neighboring cell. Similarly, a Boltzmann cell would assume a Maxwellian VDF in a neighboring Euler cell. The first-order Euler scheme uses only a two-cell stencil ($x_{i,j}$ and $x_{i+1,j}$ or $x_{i-1,j}$ and $x_{i,j}$), while the second-order discretization uses a three-cell stencil ($x_{i-1,j}$, $x_{i,j}$, and $x_{i+1,j}$) with one of the three available limiters.

The kinetic NS solver is also based on the solution of the Boltzmann equation, although, in a somewhat different fashion [22]. It is taken from the BGK model:

$$\frac{\partial f}{\partial t}+\nabla_{\mathbf{r}}\cdot(\xi f)=\frac{f^{\mathrm{eq}}-f}{\tau} \tag{11}$$

where the intercollision relaxation time τ is defined as $\tau=\mu/p$. Although not used in this study, Xu extended the use of the gas-kinetic BGK NS solver to the continuum transition regime, using a generalized definition for the collision time τ [23]. The BGK model has been found to be useful in approximating the collision integral, essentially describing how a gas in nonequilibrium relaxes to a state of equilibrium. Thus, one of the drawbacks of the BGK model is that it loses accuracy or validity as the departure from nonequilibrium increases. Xu and Guo extended the BGK model further into the nonequilibrium regime by replacing the one-stage BGK collision model with a two-stage model [24]. Another aspect of the molecular model that should be considered is the intermolecular potential. When solving the Boltzmann equation, one usually must define which intermolecular potential model one is using. With the BGK model, however, since the collision integral is replaced entirely, no explicit potential model is used. Rather, a certain collision model is specified in the calculation of τ.

A directional splitting method is used to reduce these multi-dimensional equations to a set of one-dimensional equations and then solved analytically [22]. For a one-dimensional case, the VDF is solved to be

$$f(x,\xi,t)=e^{-t/\tau}f_0(x-\xi_x t,\xi,0)+\frac{1}{\tau}\int_0^t f^{\mathrm{eq}}(x_l,\xi,t_l)e^{-(t-t_l)/\tau}\,\mathrm{d}t_l \tag{12}$$

where the trajectory of the particles x_l is calculated as $x_l=x-u(t-t_l)$, and the functional dependencies on y and z have been omitted. The VDF is calculated for each cell I with faces $i+1/2$ and $i-1/2$, with the VDF at some initial moment f_0:

$$\begin{aligned}f_0=f(x,\xi,t=0)&=f_l^{\mathrm{eq}}[1+a_l x-\tau(a_l\xi_x+A_l)](1-H[x])\\ &+f_r^{\mathrm{eq}}[1+a_r x-\tau(a_r\xi_x+A_r)]H[x]\end{aligned} \tag{13}$$

and the equilibrium VDF f_{eq} is calculated from

$$f^{\mathrm{eq}}=f_0^{\mathrm{eq}}[1+(1-H[x])\bar{a}_l x+H[x]\bar{a}_r x+At]$$

where

$$\begin{bmatrix} a_{l,r} \\ \bar{a}_{l,r} \\ A_{l,r} \\ A \end{bmatrix} = \begin{bmatrix} \alpha^1_{l,r} & \alpha^2_{l,r} & \alpha^3_{l,r} & \alpha^4_{l,r} & \alpha^5_{l,r} \\ \bar{\alpha}^1_{l,r} & \bar{\alpha}^2_{l,r} & \bar{\alpha}^3_{l,r} & \bar{\alpha}^4_{l,r} & \bar{\alpha}^5_{l,r} \\ A^1_{l,r} & A^2_{l,r} & A^3_{l,r} & A^4_{l,r} & A^5_{l,r} \\ A^1 & A^2 & A^3 & A^4 & A^5 \end{bmatrix} \begin{bmatrix} 1 \\ \xi_x \\ \xi_y \\ \xi_z \\ \xi_x^2 + \xi_y^2 + \xi_z^2 \end{bmatrix} \tag{14}$$

are polynomial functions of the local constants $\alpha^i_{l,r}$, $\bar{\alpha}^i_{l,r}$, $A^i_{l,r}$, and A^i ($i = 1, 2, 3, 4, 5$), and $f_0^{\text{eq}} = f^{\text{eq}}(x, \xi, t = 0)$, which are all determined by the method given by Li et al. [25].

Nonequilibrium is accounted for in the VDF with the terms $\tau f_l^{\text{eq}}(a_l \xi_x + A_l)$ and $\tau f_r^{\text{eq}}(a_r \xi_x + A_r)$ in Eq. (13). As long as $\tau f_{l,r}^{\text{eq}}(a_{l,r} \xi_x + A_{l,r}) \ll 1$, the approximation given here for the VDF is consistent with the first-order Chapman–Enskog expansion, and therefore recovers the NS equations.

If a NS cell has a neighbor Boltzmann cell, then the NS cell is given a velocity grid identical to the neighboring cell, and the VDF $f_0 = f_{l,r}^{\text{eq}}[1 - \tau(a_{l,r}\xi_n + A_{l,r})]$ is created on the cell interface. Using the macroparameters from the NS cell, $f_{l,r}^{\text{eq}}$ is calculated, and the coefficients for $a_{l,r}$ and $A_{l,r}$ are obtained using gradients of macroparameters from both cells. The Courant–Friedrichs–Lewy (CFL) condition is used to determine the time step for both the Euler and NS solvers. Since all of the simulations presented in this work are unsteady, each cell uses the same time step (the minimum time step for the entire domain). The CFL condition is

$$\Delta t = \frac{\text{CFL} \times h}{\max(|U + 3\sqrt{T}|, |U - 3\sqrt{T}|)} \tag{15}$$

where the nondimensional flow velocity U is defined as $U^2 = u^2 + v^2 + w^2$, and

$$\max(|U + 3\sqrt{T}|, |U - 3\sqrt{T}|) = |\xi_{\max}|$$

for the Boltzmann solver. The CFL is typically set to 0.5.

A well-known consequence of the BGK model is that the Prandtl number can only be unity [26], $Pr = c_p \mu / k = 1$. Thus, when using the BGK model, which includes the kinetic-based NS solver discussed previously, one can accurately model either the viscosity μ or the coefficient of thermal conductivity k but not both. Xu presents a Prandtl number fix based on altering the heat flux Q [22]. The energy flux is modified by adding the correction term $(Pr^{-1} - 1)Q$ to it, where Q is calculated on the cell faces, using polynomial interpolation of the VDF, and Pr is a variable Prandtl number. Results have been reported for shock wave structure by May et al. [27] and Xu [22], showing that the regular NS solver (based on fluid continuum assumptions) and the kinetic-based NS solver show good agreement.

Since UFS is a hybrid code, it has kinetic solvers in addition to the kinetic-based continuum solvers. The kinetic solver used in this work is the BGK model. However, since the BGK model does not calculate a collision integral, it does not inherently have the capability to account for internal molecular energies, and is therefore only used for the argon simulations. To retain the computational efficiency of the BGK model, UFS uses a three-temperature BGK (3T-BGK) model for flows involving internal energies (used for the N_2 simulations), as described in [28]. The 3T-BGK model assumes that there is a translational temperature T_{tr}, a rotational temperature T_{rot}, and a vibrational temperature T_{vib}. Josyula et al. [29] used a 3T-BGK model as well, but the three temperatures were translational temperatures in the coordinate directions. Also, Josyula et al. implemented a two-temperature BGK model for the translational and rotational temperatures in [30]. The equilibrium temperature T_{eq} can be obtained from a weighted average of the temperatures with $K_r = 2$ and $K_v = 3$ for N_2,

$$T^{\text{eq}} = (3T_{\text{tr}} + K_r T_{\text{rot}} + K_v T_{\text{vib}})/(3 + K_r + K_v^{\text{eq}})$$

where $K_v^{\text{eq}} = K_v(T^{\text{eq}})$. The Maxwellian VDF f^{eq} is then calculated as $f^{\text{eq}} = f^{\text{eq}}(T_{\text{tr}}) f^{\text{eq}}(T_{\text{rot}}) f^{\text{eq}}(T_{\text{vib}})$, which assumes that the VDFs for each of the three temperatures are statistically independent of one another.

To successfully couple a continuum solver with a kinetic solver, a switching parameter is required. Schrock [5] and Carr [4] both investigated entropy generation as a means of quantifying continuum breakdown. The switching parameter used in the first part of this work is

$$S_{\text{NS}} = Kn \sqrt{\left(\frac{\nabla p}{p}\right)^2 + \frac{1}{U^2}\left[\left(\frac{\partial u}{\partial x}\right)^2 + \left(\frac{\partial v}{\partial y}\right)^2 + \left(\frac{\partial w}{\partial z}\right)^2\right]} \tag{16}$$

where all values are nondimensional. S_{NS} has been shown by Kolobov et al. to correctly couple the solvers near a shock wave at moderate Knudsen numbers [2]. A user-specified threshold value for S_{NS} is provided in an input file, and S_{NS} is calculated for each cell. If a cell's value for S_{NS} is larger than the threshold, then that cell is flagged as a Boltzmann cell. Otherwise, it is flagged as a continuum cell. Thus, by decreasing the S_{NS} threshold value, one decreases the number of continuum cells in the domain, while increasing the threshold value makes the Boltzmann region(s) smaller. For this study, the threshold value used is based on the density gradient and local Knudsen number ($S_\rho = Kn|\nabla p|/p$), since the entropy spot has an accompanying density fluctuation profile [2,31].

III. Entropy-Shock Interaction Problem Initialization

Based on previous works [6,16,17], a Gaussian entropy spot was chosen of the form $T_1'/T_1 = \varepsilon e^{-r^2/2}$, shown in Fig. 1a, with a perturbation amplitude of $\varepsilon = 0.25$, and the radius from the center of the entropy spot r is calculated from $r^2 = (x - x_c)^2 + (y - y_c)^2$. The local density is then calculated as $\rho_1 + \rho_1' = p_1/(T_1 + T_1')$, shown in Fig. 1b, noting that the pressure is constant in an entropy spot, while the density and temperature fluctuate. Even though the maximum temperature fluctuation is 25%, the minimum density fluctuation is only −20%.

A schematic diagram of the overall computational problem setup is shown in Fig. 2. A closer, qualitative view of the initial computational grid and density contours for the entropy spot initialization is found in Fig. 3. The density contours represented in Fig. 3 range from a minimum of $\rho_{\min} = 0.80$ kg/m^3 to a maximum of $\rho_{\max} = 1.00$ kg/m^3, although the actual maximum density in the computational domain occurs behind the shock at $\rho = 2.51$ kg/m^3.

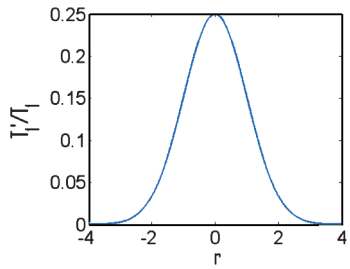

a) Temperature

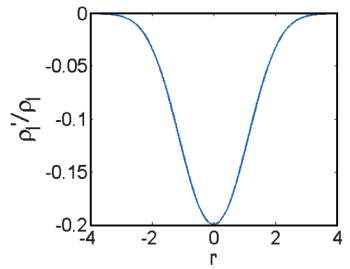

b) Density

Fig. 1 Entropy spot temperature and density profiles.

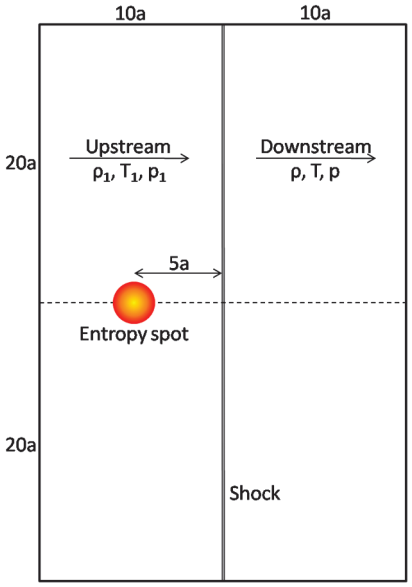

Fig. 2 Grid setup for entropy-shock simulation at $t = 0$ (adapted from [17]).

The full computational grid setup is one rectangle with dimensions of $20a \times 40a$, where the radius of the entropy spot a is chosen to be $25\lambda_1$. The radius and exterior domain dimensions were chosen to be similar to those conditions presented in [6,16,17]. The top and bottom boundaries are freestream boundaries. The upstream Mach number is $M_1 = 2.0$, with the flow propagating from the left to the right. The center of the entropy spot is initially located five radii upstream of the shock in the middle of the vertical domain.

The flowfield is initialized in argon with upstream and downstream values based on the Rankine–Hugoniot shock jump conditions, and then the shock is allowed to develop with just the NS solver, after which the shock is allowed to develop with the coupled BGK and NS solvers ($S_\rho = 0.01$) until it achieves a steady state ($Pr = 2/3$, molecular mass is 39.948 atomic mass units, molecular diameter is 4.17×10^{-10} m, $T_1 = 300$ K, $\rho_1 = 6.63 \times 10^{-6}$ kg/m^3, and $\lambda_1 =$ 0.01721 m). Once the flowfield is thus computed (taken as $t = 0$), the entropy spot is inserted upstream and allowed to freely convect through the shock, using the coupled BGK and NS solvers. Figure 3 shows the computational domain (colored by density) immediately after the entropy spot is introduced for $Kn = 0.1$.

Three Knudsen numbers are investigated in order to study the effects of rarefaction on entropy-shock interactions. The Knudsen numbers were chosen to be within the continuum ($Kn = 0.01$), near-continuum ($Kn = 0.1$), and rarefied regimes ($Kn = 1.0$).

Grid studies in physical space were conducted on coarse, medium, and fine grids. The medium grid is refined up to level 10 ($\Delta_0 = 500\lambda_1$ and $\Delta_{10} \approx \lambda_1/2$), based on the spatial gradient of ($\ell_n \rho + \ell_n p$). The gradient of the natural logarithm of density and pressure is used as a basis for grid definition in order to converge the grid on both density and pressure fluctuations; this is an extension of the method used in [2], using density as the sole criterion to resolve density variations. For the x direction, if any cell has a gradient of the form

$$\partial/\partial x(\ell_n \rho + \ell_n p) = (1/\rho)(\partial\rho/\partial x) + (1/p)(\partial p/\partial x)$$

larger than 0.01 (or of 1%), then it is refined until either the gradient is less than 0.01 or it is refined to level 10, whichever occurs first. The coarse grid is refined up to level 9 ($\Delta_9 \approx \lambda_1$), and the fine grid is refined to level 11 ($\Delta_{11} \approx \lambda_1/4$), with the same criterion on the gradient. The rarefied simulations ($Kn = 1.0$) had to be computed using only the coarse grid. At a value of $Kn = 1.0$, the medium and fine grids were unsuitable, due to the low molecular number density in each cell, since the molecular number density decreases with increasing Kn. For $Kn = 0.01$, the density profiles agree within 3% between the fine and medium grids. For $Kn = 0.1$, the density profiles agree within 1% between the coarse and medium physical grids. Again, no grid study was performed for $Kn = 1.0$, since the coarse grid was the finest grid that could be used.

Velocity-space grid studies were also performed on coarse, medium, and fine grids. All of the grids have ranges of $-4V_{\text{ref}}$ to $6V_{\text{ref}}$ in the u direction, and $-5V_{\text{ref}}$ to $5V_{\text{ref}}$ in the v direction. The coarse grid has 10×10 nodes, the medium grid has 20×20 nodes, and the fine grid has 40×40 nodes. The node spacing is then V_{ref}, $0.5V_{\text{ref}}$, and $0.25V_{\text{ref}}$ for the coarse, medium, and fine grids, respectively. For $Kn = 0.01$ and 0.1, the density profiles agree within 0.1% between the fine and medium grids. No velocity grid study was performed for $Kn = 1.0$ for the same rarefaction effect mentioned in the previous paragraph.

In the next section, gradient profiles are presented for density, pressure, and temperature. A second-order scheme is used to compute the gradients as before, $\partial b/\partial x = (b_{i+1} - b_{i-1})/2\Delta x + O(\Delta x^2)$, where b represents density, pressure, or temperature. However, no VDFs are presented, since the only cells that output the VDF are Boltzmann cells, which are primarily in the shock structure alone.

IV. Entropy-Shock Interaction Results

The midpoint of the shock, based on density, moves as the entropy spot convects through the shock, and the entire shock actually is bowed, however, slightly. Figure 4 gives the change in shock location

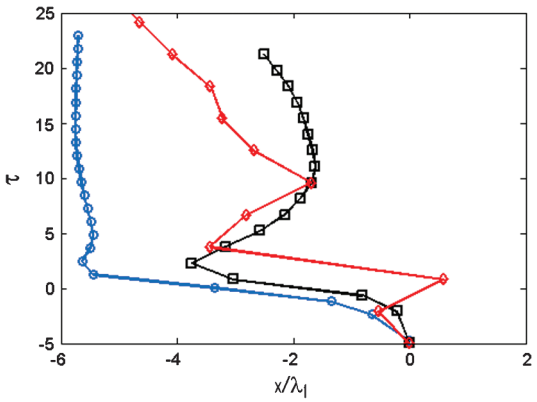

Fig. 4 Shock locations as the simulation progresses in time τ for all three Knudsen numbers: $Kn = 0.01$ (blue), 0.1 (black), and 1.0 (red).

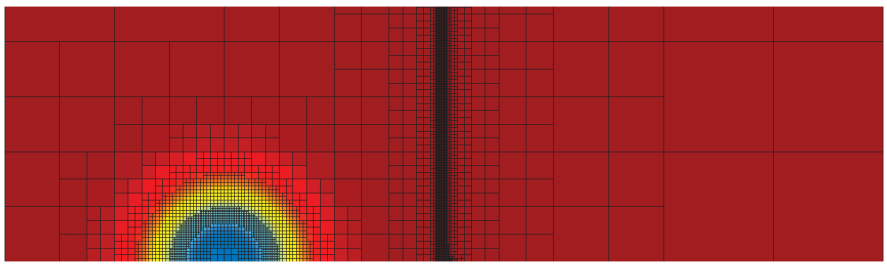

Fig. 3 Density contours for entropy spot initialization in front of the shock in the computational domain, where $\rho_{\min} = 0.80$ (blue), and $\rho_{\max} = 1.00$ (red). $Kn = 0.1$ medium physical and velocity grids (grid dimensions are $20a \times 5a$).

for all three Knudsen numbers, where the nondimensional time τ equals zero when the center of the entropy spot passes through $x/\lambda_1 = 0$. Since the center of the entropy spot is $5a$ upstream of the shock, τ is calculated as [6]:

$$\tau \equiv \frac{t - 5(a/u_1)}{(a/u_1)} \tag{17}$$

Qualitatively, the shock location profiles exhibit similar behaviors. Even at $Kn = 0.01$, which is well into the continuum regime, the shock experiences a restoring force toward $x/\lambda_1 = 0$, albeit a small one. The shock does not return to its equilibrium location (as a completely normal shock) at any of the Knudsen numbers, because the pressure wave, which emanates from the entropy spot after it has impinged with the shock, causes the shock to be bowed upstream.

The density, pressure, and temperature profiles, as well as their gradient profiles, are shown in Figs. 5–7 for three different Knudsen numbers: $Kn = 0.01$, 0.1, and 1.0. For $Kn = 0.01$, the density fluctuation is initially unaffected by the shock, with a postshock strength of -20% at $\tau = 1.0$, damping out to -14% by $\tau = 20.3$. It is possible that, with such a low Knudsen number, the shock thickness is not allowing the density fluctuation sufficient time to change. The temperature fluctuation, however, is initially affected by the shock, which has a postshock strength of only 20% (compared with a preshock strength of 25%) at $\tau = 2.2$, damping out to 14% at $\tau = 20.3$. It is interesting to note that, even though the entropy spot

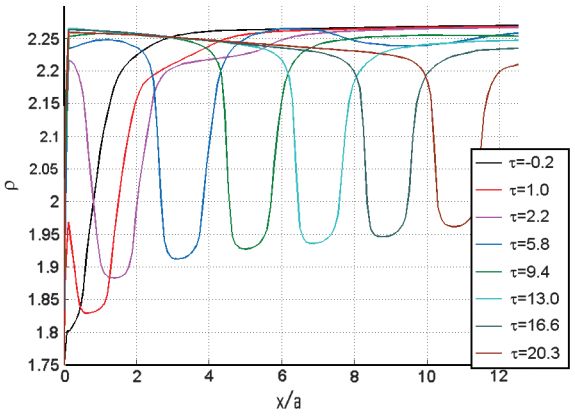

a) Density

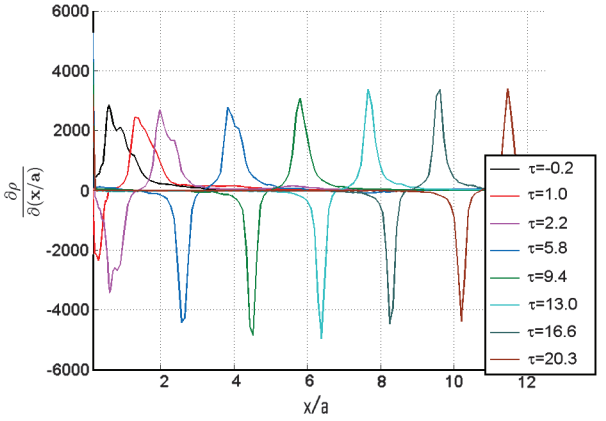

b) Density gradients

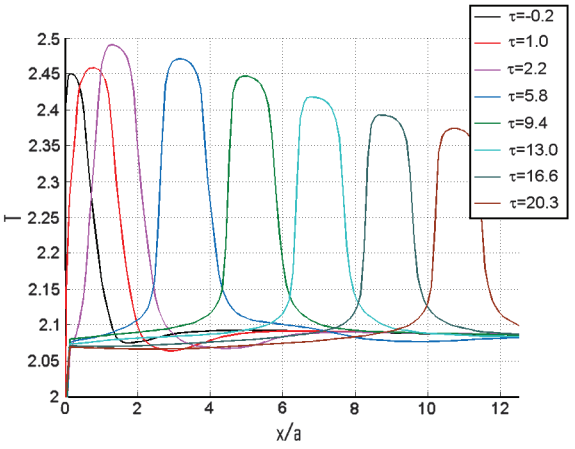

c) Temperature

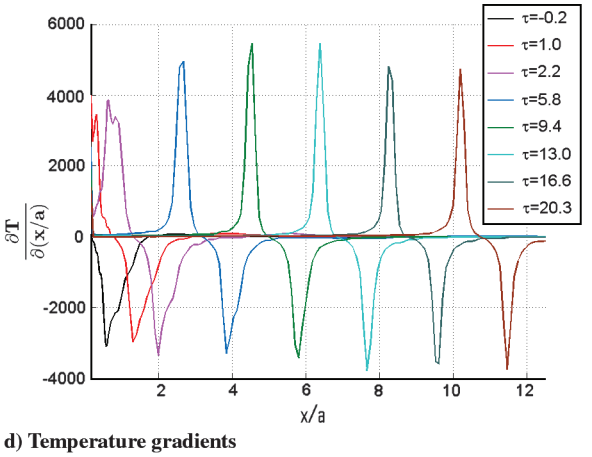

d) Temperature gradients

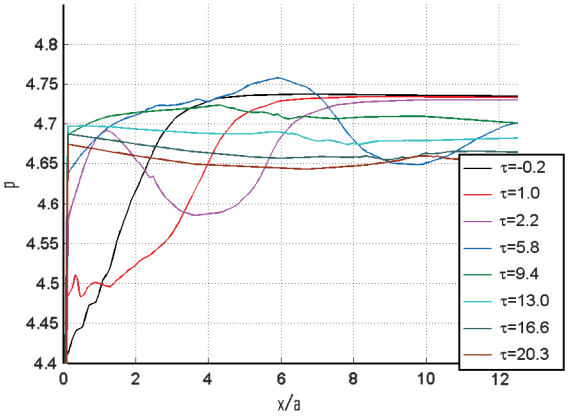

e) Pressure

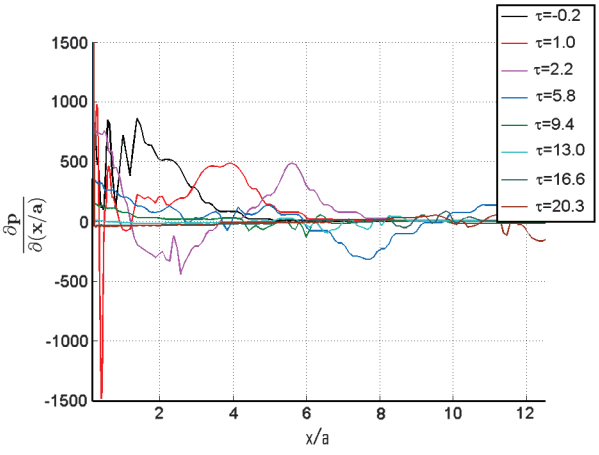

f) Pressure gradients

Fig. 5 Profiles for $Kn = 0.01$.

does not induce any pressure fluctuations upstream of the shock, by convecting through the shock, the interaction creates a circular pressure wave centered about the symmetry plane [6]. The pressure profile in Fig. 5 shows a minimum of -6% at $\tau = 1.0$, which dampens to a minimum of -2% at $\tau = 5.8$. For $\tau > 5.8$, the pressure profile shows that there is a rarefaction region at the symmetry line, since the pressure is decreased by as much as 2% at $\tau = 20.3$. The numerical error introduced by the shock-symmetry boundary interface is apparent here near $x/a = 0$, since the flow parameters are relaxing from values above the downstream equilibrium values.

For $Kn = 0.1$, the shock thickness is larger than the simulation with $Kn = 0.01$. As a result, the density fluctuation is more affected initially by the shock, with a postshock strength of -19% at $\tau = 0.8$, damping out to -8% by $\tau = 18.3$. The strength of the temperature fluctuation is cut to 17% at $\tau = 0.8$, damping out to 10% at $\tau = 18.3$. The pressure shows a minimum of -1.4%, with a maximum of 0.8%, both at $\tau = 5.2$. This result indicates that an expansion wave is immediately followed by a compression wave. For $\tau > 5.2$, the pressure profile indicates that there is actually a compression region after the shock at $Kn = 0.1$, which is in contrast to the rarefaction region predicted for $Kn = 0.01$.

For $Kn = 1.0$, the shock thickness is larger still, apparent from the attenuation of the density fluctuation downstream of the shock (-7% at $\tau = 0.8$, dampened to -3% at $\tau = 9.6$). The strength of the temperature fluctuation is now only 8% at $\tau = 0.8$, damping out to 4% by $\tau = 9.6$. The pressure is actually exhibiting values above the

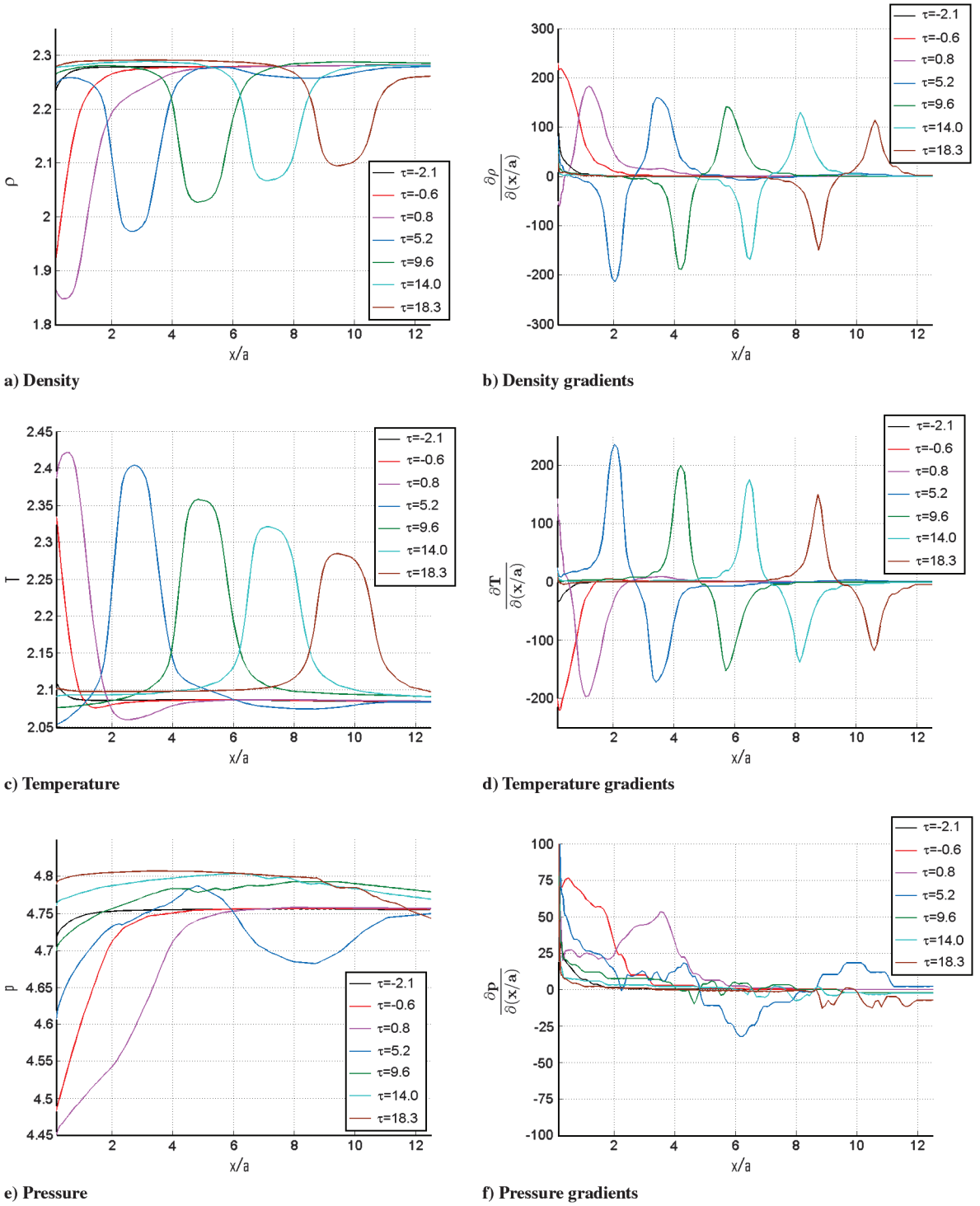

a) Density

b) Density gradients

c) Temperature

d) Temperature gradients

e) Pressure

f) Pressure gradients

Fig. 6 Profiles for $Kn = 0.1$.

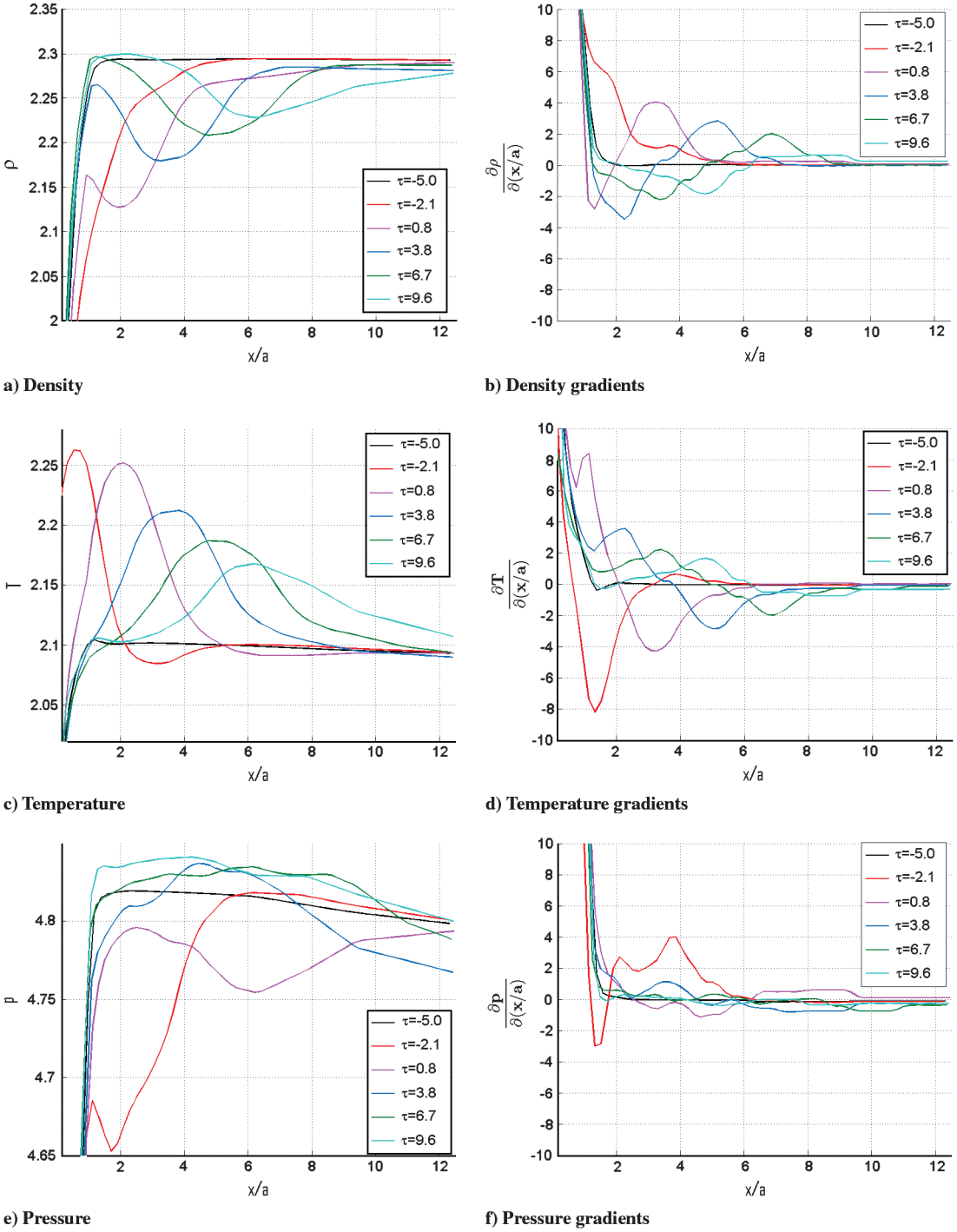

a) Density

b) Density gradients

c) Temperature

d) Temperature gradients

e) Pressure

f) Pressure gradients

Fig. 7 Profiles for $Kn = 1.0$.

downstream equilibrium value by 1% at $\tau = 0.8$ and 2% by $\tau = 9.6$, suggesting a compression region downstream of the shock.

V. Conclusions

Entropy-shock interactions continue to be an area of research, with the work presented here extending the state of the art to an analysis with NS and kinetic schemes. The shock moves upstream, due to entropy-shock interactions, and never recovers to a normal shock. Also, for $Kn = 0.01$, a rarefaction region is observed downstream of the shock, while for $Kn = 0.1$ and 1.0, a compression region is given. As CFD Research Corporation improves the capabilities of UFS, especially the visualization software, the pressure waves downstream of the shock may be studied using pressure contours. VDFs may be studied by using a smaller value for the continuum breakdown parameter or by performing the simulations with an uncoupled kinetic solver. The authors also recommend that the UFS solver be improved to include a DSMC Boltzmann solver. Such an option would provide greater flexibility in solving flows such as the ones presented in this study.

Acknowledgments

This work would not have been possible without the guidance and funding of Datta Gaitonde and Eswar Josyula of the Air Vehicles Directorate of the U.S. Air Force Research Laboratory. Robert Arslanbekov and Vladimir Kolobov of the CFD Research Corporation provided indispensable comments regarding the use of the unified flow solver, as well as the code required to introduce an entropy spot during a simulation.

References

[1] Kolobov, V., Aristov, V., Arslanbekov, R. R., Bayyuk, S., Frolova, A., and Zabelok, S., "Construction of a Unified Continuum/Kinetic Solver for Aerodynamic Problems," *Journal of Spacecraft and Rockets*, Vol. 42, No. 4, 2005, pp. 598–606. doi:10.2514/1.10468

[2] Kolobov, V. I., Arslanbekov, R. R., Aristov, V. V., Frolova, A. A., and Zabelok, S. A., "Unified Solver for Rarefied and Continuum Flows with Adaptive Mesh and Algorithm Refinement," *Journal of Computational Physics*, Vol. 223, No. 2, 2007, pp. 589–608. doi:10.1016/j.jcp.2006.09.021

[3] Kolobov, V. I., Arslanbekov, R. R., Aristov, V. V., Frolova, A. A., and Zabelok, S. A., "Unified Flow Solver for Aerospace Applications," 44th AIAA Aerospace Sciences Meeting and Exhibit, AIAA Paper 2006-988, 2006.

[4] Carr, R. W., "Quantifying Non-Equilibrium in Hypersonic Flows Using Entropy Generation," M.S. Thesis, Department of Aeronautics and Astronautics, Air Force Institute of Technology, Wright-Patterson AFB, OH, 2007.

[5] Schrock, C. R., "Entropy Generation as a Means of Examining Continuum Breakdown," M.S. Thesis, Department of Aeronautics and Astronautics, Air Force Institute of Technology, Wright-Patterson AFB, OH, 2007.

[6] Grasso, F., and Pirozzoli, S., "Shock Wave–Termal Inhomogeneity Interactions: Analysis and Numerical Simulations of Sound Generation," *Physics of Fluids*, Vol. 12, No. 1, 2000, pp. 205–219. doi:10.1063/1.870296

[7] Anyiwo, J. C., and Bushnell, D. M., "Turbulence Amplification in Shock-Wave Boundary-Layer Interaction," *AIAA Journal*, Vol. 20, No. 7, 1982, pp. 893–899. doi:10.2514/3.7954

[8] Hussaini, M. Y., Collier, F., and Bushnell, D. M., "Turbulence Alteration due to Shock Motion," *Turbulent Shear-Layer/Shock-Wave Interactions*, Springer–Verlag, New York, 1986, pp. 371–381.

[9] McKenzie, J. F., and Westphal, K. O., "Interaction of Linear Waves with Oblique Shock Waves," *Physics of Fluids*, Vol. 11, No. 11, 1968, pp. 2350–2362. doi:10.1063/1.1691825

[10] Meadows, K., Kumar, A., and Hussaini, M., "A Computational Study on the Interaction Between a Vortex and a Shock Wave," AIAA 12th Aeroacoustics Conference, AIAA Paper 89-1043, 1989.

[11] Moore, F. K., "Unsteady Oblique Interaction of a Shock Wave with a Plane Disturbance," NACA TR 1165, 1954.

[12] Ribner, J. S., "Convection of a Pattern of Vorticity Through a Shock Wave," NACA TR 1164, 1954.

[13] Zang, T. A., Hussaini, M. Y., and Bushnell, D. M., "Numerical Computations of Turbulence Amplification in Shock-Wave Interactions," *AIAA Journal*, Vol. 22, No. 1, 1984, pp. 13–21. doi:10.2514/3.48414

[14] Duck, P. W., Lasseigne, D. G., and Hussaini, M. Y., "On the Interaction Between the Shock Wave Attached to a Wedge and Freestream Disturbances," *Theoretical and Computational Fluid Dynamics*, Vol. 7, No. 2, 1995, pp. 119–139. doi:10.1007/BF00311809

[15] Duck, P. W., Lasseigne, D. G., and Hussaini, M. Y., "The Effect of Three-Dimensional Freestream Disturbances on the Supersonic Flow Past a Wedge," NASA CR 201698, 1997.

[16] Fabre, D., and Jacquin, L., "Linear Interaction of a Cylindrical Entropy Spot with a Shock," *Physics of Fluids*, Vol. 13, No. 8, 2001, pp. 2403–2422. doi:10.1063/1.1383592

[17] Hussaini, M. Y., and Erlebacher, G., "Interaction of an Entropy Spot with a Shock," *AIAA Journal*, Vol. 37, No. 3, 1999, pp. 346–356. doi:10.2514/2.736

[18] Grasso, F., and Pirozzoli, S., "Shock-Wave–Vortex Interactions: Shock and Vortex Deformations, and Sound Production," *Theoretical and Computational Fluid Dynamics*, Vol. 13, No. 6, 2000, pp. 421–456. doi:10.1007/s001620050121

[19] Bentley, B. I., "An Investigation of Shock Wave Physics via Hybrid CFD-BGK Solution Methods for Nonequilibrium Flows," M.S. Thesis, Department of Aeronautics and Astronautics, Air Force Institute of Technology, Wright-Patterson AFB, OH, 2009.

[20] Harris, S., *An Introduction to the Theory of the Boltzmann Equation*, Dover, Mineola, NY, 1971.

[21] Sone, Y., *Kinetic Theory and Fluid Dynamics*, Birkhäuser, Boston, 2002.

[22] Xu, K., "A Gas-Kinetic BGK Scheme for the Navier–Stokes Equations and its Connection with Artificial Dissipation and Godunov Method," *Journal of Computational Physics*, Vol. 171, No. 1, 2001, pp. 289–335. doi:10.1006/jcph.2001.6790

[23] Xu, K., "Regularization of the Chapman–Enskog Expansion and its Description of Shock Structure," *Physics of Fluids*, Vol. 14, No. 4, 2002, L17. doi:10.1063/1.1453467

[24] Xu, K., and Guo, Z., "Generalized Gas Dynamic Equations," 47th AIAA Aerospace Sciences Meeting Including The New Horizons Forum and Aerospace Exposition, AIAA Paper 2009-672, 2009.

[25] Li, Q., Fu, S., and Xu, K., "A Compressible Navier–Stokes Flow Solver with Scalar Transport," *Journal of Computational Physics*, Vol. 204, No. 2, 2005, pp. 692–714. doi:10.1016/j.jcp.2004.10.026

[26] Vincenti, W. G., and Kruger, C. H., *Introduction to Physical Gas Dynamics*, 1st ed., Krieger, Malabar, FL, 1975.

[27] May, G., Srinivasan, B., and Jameson, A., "An Improved Gas-Kinetic BGK Finite-Volume Method for Three-Dimensional Transonic Flow," *Journal of Computational Physics*, Vol. 220, No. 2, 2007, pp. 856–878. doi:10.1016/j.jcp.2006.05.027

[28] Arslanbekov, R. R., Kolobov, V. I., Frolova, A., Zabelok, S., and Josyula, E., "Evaluation of a Unified Kinetic/Continuum Solver for Computing Heat Flux in Hypersonic Blunt Body Flows," 39th AIAA Thermophysics Conference, AIAA Paper 2007-4544, 2007.

[29] Josyula, E., Xu, K., and Wadsworth, D. C., "Testing Continuum and Non-Continuum Descriptions in High Speed Flows," *AIP Conference Proceedings*, Vol. 762, American Inst. of Physics, Melville, NY, 2005, pp. 1217–1222. doi:10.1063/1.1941699

[30] Josyula, E., Bailey, W. F., and Xu, K., "Nonequilibrium Relaxation in High Speed Flows," 37th AIAA Thermophysics Conference, AIAA Paper 2004-2468, 2004.

[31] Roveda, R., Goldstein, D. B., and Varghese, P. L., "Hybrid Euler/Direct Simulation Monte Carlo Calculation of Unsteady Slit Flow," *Journal of Spacecraft and Rockets*, Vol. 37, No. 6, 2000, pp. 753–760. doi:10.2514/2.3647